Article

Assessing radiometric correction approaches for multi-spectral UAS imagery for horticultural applications

Yu-Hsuan Tu [1,*], Stuart Phinn [1], Kasper Johansen [2] and Andrew Robson [3]

[1] Remote Sensing Research Centre, School of Earth and Environmental Sciences, The University of Queensland, St Lucia, QLD, 4072 Australia; y.tu@uq.edu.au; s.phinn@uq.edu.au
[2] Hydrology, Agriculture and Land Observation Group, Water Desalination and Reuse Center, King Abdullah University of Science and Technology, Thuwal, 23955-6900, Kingdom of Saudi Arabia; kasper.johansen@kaust.edu.sa
[3] Precision Agriculture Research Group, School of Science and Technology, University of New England, Armidale, NSW, 2351 Australia; andrew.robson@une.edu.au
* Correspondence: y.tu@uq.edu.au; Tel.: +61-7-3346-7023

Abstract: UAS-based multi-spectral imagery is becoming increasingly popular for the improved monitoring and managing of various horticultural crops. However, for UAS data to be used as an industry standard for assessing tree structure and condition as well as production parameters, it is imperative that the appropriate data collection and pre-processing protocols are established to enable multi-temporal comparison. There are several UAS-based radiometric correction methods commonly used for precision agricultural purposes. However, their relative accuracies have not been assessed for data acquired in complex horticultural environments. This study assessed the variations in estimated surface reflectance values of different radiometric corrections applied to multi-spectral UAS imagery acquired in both avocado and banana orchards. We found that inaccurate calibration panel measurements, inaccurate signal-to-reflectance conversion, and high variation in geometry between illumination, surface, and sensor viewing produced significant radiometric variations in at-surface reflectance estimates. Potential solutions to address these limitations included appropriate panel deployment, site-specific sensor calibration, and appropriate BRDF correction. Future UAS based horticultural crop monitoring can benefit from the proposed solutions to radiometric corrections to ensure they are using comparable image-based maps of multi-temporal biophysical properties.

Keywords: UAS; multi-spectral imagery; radiometric correction; BRDF; horticulture

1. Introduction

UAS-based multi-spectral imagery is becoming commonly used for monitoring and managing horticultural crops [1-6]. One of the final products from common commercially available image processing applications is an ortho-rectified mosaic with digital number values [5-7]. Although such images are sufficient for some types of classification [6-8], the digital numbers only represent the relative brightness range of the ground features and cannot be used to extract consistent information on biophysical properties, derive calibrated vegetation indices or be used to compare multi-temporal datasets. Therefore, the orthomosaic imagery needs to be converted from digital number to normalised at-surface reflectance [8,9].

In past studies, one of the most common ways to correct the imagery from digital numbers to at-surface reflectance has been the simplified empirical approach [4,10,11]. The idea of the empirical method is to identify the relationship between known reflectance targets within the extent of an image to their measured digital number. The best-fit equation produced from this relationship is then

Peer-reviewed version available at *Remote Sens.* **2018**, *10*, 1684; doi:10.3390/rs10111684

used to convert all digital numbers within the image to at-surface reflectance values. A novel correction method to generate an orthomosaiced reflectance image directly without the need for an empirical correction has been developed in recent years for calibrating Parrot Sequoia® (Parrot Drone SAS, Paris, Frence) and MicaSense RedEdge® (MicaSense Inc, Seattle, USA) multi-spectral imagery. The function in the Pix4DMapper software (Pix4D S.A., Lucerne, Switzerland) is called 'reflectance map' while a similar function is called 'calibrate reflectance' in Agisoft PhotoScan Pro (Agisoft LLC, St. Petersburg, Russia), which uses several photograph parameters to calculate reflectance [12]. In terms of correcting for variations in illumination, software packages such as Agisoft PhotoScan Pro and Pix4DMapper provide 'colour correction/balancing' features to implement the image-information-based radiometric block adjustment algorithm. Yet such algorithms only consider the homogeneity of adjacent images' histogram regardless of the Bidirectional Reflectance Distribution Function (BRDF) effect within a single image. Moreover, studies have also stated that irradiance normalisation and BRDF correction are essential for time-series applications and estimation of biophysical properties [13,14], yet they are not included features in any commercial UAS processing software packages.

Another issue that has not been addressed in UAS image-based radiometric correction is selection of the most robust normalisation process. Traditionally, various parameters are considered for normalisation when processing satellite images, including solar, topographic, and viewing geometries and Sun-Earth distance [8]. As for aerial imagery, the increasing spatial resolution and smaller frame size can cause a higher spectral variance in features information, especially in complex forest environments [15-17]. The increasing spatial resolution amplifies observed topographic and BRDF effects within and between image scenes, as the non-uniformity of natural surfaces becomes more obvious at finer scales [16,17]. When coupled with increased variability in measured spectral reflectance observed at smaller pixel sizes, this creates a substantive problem for effective radiometric normalisation. In a highly dynamic platform such as UAS, ineffective normalisation may cause the data being not comparable in multi-temporal domain.

This study assesses radiometric correction algorithms for UAS imagery provided from commercially available software packages. The application of BRDF corrections are also investigated. While radiometric correction approaches of satellite and airborne imagery are well established, there is a significant lack of protocols and comparison of methods for radiometrically correcting UAS-based imagery. Our research addresses this gap in knowledge with specific focus on horticultural environments.

2. Materials and Methods

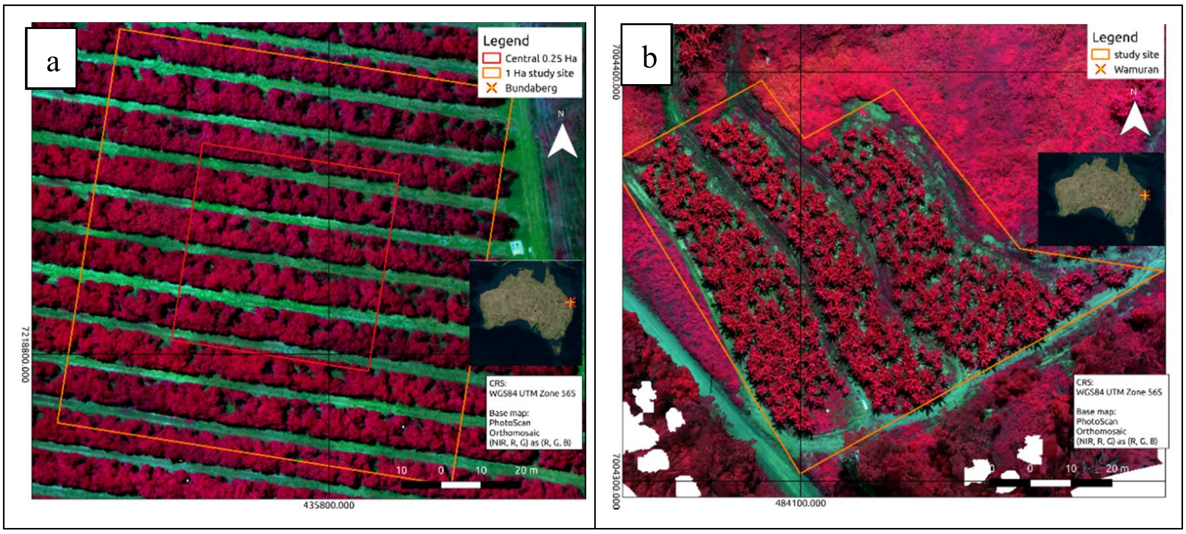

Figure 1 Study sites: (a) Avocado orchard in Bundaberg, (b) banana orchard in Wamuran.

Peer-reviewed version available at *Remote Sens.* **2018**, *10*, 1684; doi:10.3390/rs10111684

2.1 Study sites

The two study sites were located in Queensland, Australia. The avocado orchard was located to the south of Bundaberg, which is one of the main avocado producing regions of Australia. The banana plantation was located in Wamuran in the Sunshine Coast hinterland of South East Queensland. The UAV based focus areas encompassed 1 and 0.5 ha patches of the avocado and banana orchards, respectively (Figure 1). The average elevation for the avocado orchard was around 60 m above sea level, relatively flat terrain with an average slope of 4 degrees. The banana plantation was located on a hill slope with an elevation varying from 113 m to 170 m above sea level and an average slope of 21 degrees.

2.2. UAS data acquisition

Five UAS flight datasets, including three for the avocado orchard and two for the banana orchard, were captured with a Parrot Sequoia multi-spectral camera mounted on a 3DR Solo (3D Robotics, Berkeley, USA) quadcopter under clear sky conditions. The camera acquires imagery in the green (550 nm, 40 nm bandwidth), red (660 nm, 40 nm bandwidth), red edge (735 nm, 10 nm bandwidth), and NIR (790 nm, 40 nm bandwidth) part of the spectrum with its 4.8 × 3.6 mm (1280 × 960 pixels) CMOS sensor. The camera is also fitted with an upward-facing irradiance sensor with the same spectral bands. The sensor can measure the arbitrary incoming irradiance for each image frame so that the irradiance measurement can be used for radiometric normalisation.

The image acquisition of the avocado trees was conducted using an established flight grid pattern, which included both along- and across- tree-row flight directions. The first flight was conducted at 75 m AGL on 2 Feb 2017 between 2:11-2:25 PM (60° solar elevation); the second flight was at 100 m AGL on 3 Feb 2017 between 12:46-12:59 PM (80° solar elevation); and the third flight was at 50 m AGL on 5 Feb 2017 between 12:34-12:40 PM (80° solar elevation).

The banana plantation in Wamuran is located in hilly terrain. Therefore, the flight pattern had to follow the direction perpendicular to the slope aspect to ensure safety and data quality. A 1 m DEM was used to design the flight plan to ensure the flight height was maintained at approximately 50 m AGL for each camera waypoint. We used the data from two flights, which were collected between 11:37-11:44 AM and between 12:11-12:17 PM on 4 Apr 2018. The sun elevation for both flights was approximately 57°. The rest of the flight settings were the same for both the avocado and banana orchard, i.e. an 80% sidelap, 1-second image capture interval (>85% forward overlap), and 5 m/s flight speed.

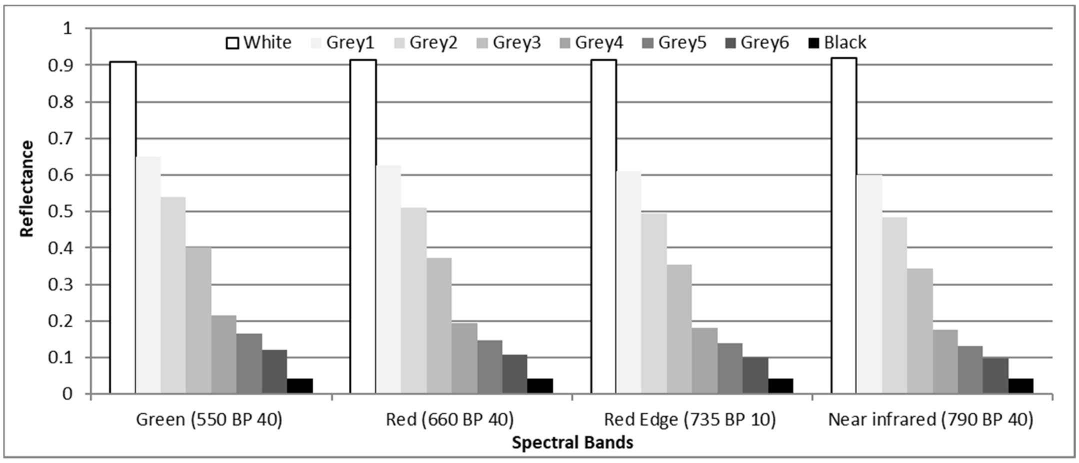

Figure 2 Measured spectral reflectance of the eight greyscale radiometric calibration panels, corresponding with the four Parrot Sequoia® multi-spectral bands using a handheld ASD visible-NIR range spectrometer.

For every dataset, 10 AeroPoints® (Propeller Aerobotics Pty Ltd, Surry Hills, Australia) were deployed as ground control points (GCPs). The locations of the AeroPoints were recorded for five hours and subsequently post-processed using the Propeller® network correction based on the nearest base station, located within 26 and 11 km of the Bundaberg and Wamuram study sites, respectively. Eight radiometric calibration panels with greyscales ranging from black to white were deployed, following the method suggested by [4] and [10]. The reflectance of the calibration panels varied from 4% to 92% in all spectral bands (**Error! Reference source not found.**). For the banana datasets only, a MicaSense® calibration panel was used to acquire calibration images for the Parrot Sequoia® camera.

2.3. Image pre-processing

2.3.1 Geometric correction and initial pre-processing

Agisoft PhotoScan Pro and Pix4DMapper were used to process the multi-spectral UAS data with the addition of in-house Python scripts. For photo alignment, a limit of 10000 tie points was used with the measured GCPs, derived from the AeroPoint® centres, imported to geometrically calibrate the images. The geo-referencing errors were 0.07 m, 0.11 m, and 0.02 m for the three avocado datasets, and 0.01 m for both banana datasets, respectively, based on the bundle-adjustment error assessment report [18]. For the Agisoft PhotoScan Pro, a noise filter was applied during point cloud generation, while for Pix4DMapper the noise filter was applied during the derivation of Digital Surface Model (DSM). Mild filtering (or sharp smoothening) was used in both workflows to preserve as much detail as possible of the tree crown structure. The final step was to ortho-rectify the image pixels to the DSM and create a mosaic. In Pix4DMapper a vignetting polynomial was used, while for Agisoft PhotoScan Pro, a distance to the surface model was developed for every pixel to simulate the radiant attenuation for vignetting correction [19-21]. The two software packages use different projection algorithms to project pixels to the DSM. The orthomosaics from Agisoft PhotoScan look closer to the original images, while the orthomosaics from Pix4DMapper often appear with a halo effect around the perimeter of tall features, e.g. trees, caused by the ortho-rectification process (Figure 3). By default, Pix4DMapper produces the orthomosaic with colour-balancing enabled, while Agisoft PhotoScan Pro did not have a function to balance brightness until version 1.3 as an optional calibration.

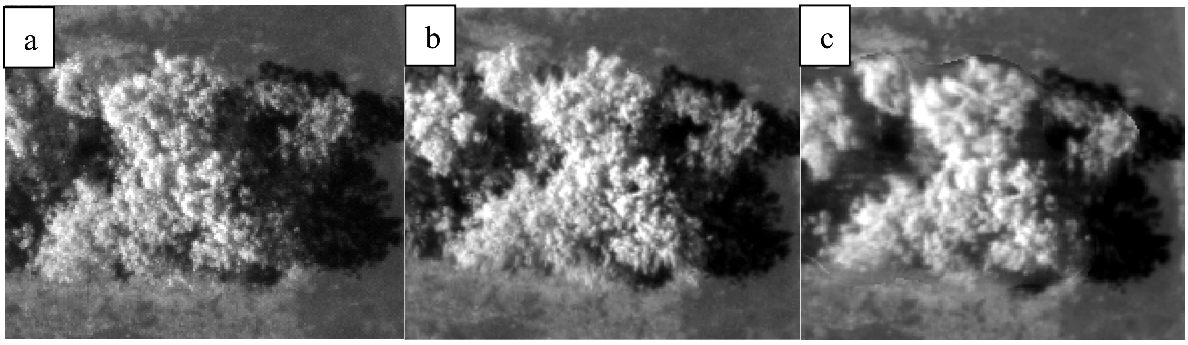

Figure 3 The appearance of the same avocado tree between (a) an original image; and the orthomosaics derived from (b) Agisoft PhotoScan and (c) Pix4DMapper. Although the avocado tree looks similar in a-c, the halo effect surrounding the tree in (c) is visible.

2.3.2 Producing analysis ready data

At-surface reflectance images were generated for each band for all datasets with four types of correction methods:

1. Simplified empirical correction;
2. Colour balancing before empirical correction;
3. Irradiance normalisation before empirical correction; and
4. Sensor-information based calibration.

The empirical correction in methods 1 to 3 was achieved using an in-house Python script to convert DN values to at-surface reflectance from the orthomosaic products based on the radiometric calibration panels. This processing workflow produced a total of 144 (4 correction methods × 3 flight

Peer-reviewed version available at *Remote Sens.* **2018**, *10*, 1684; doi:10.3390/rs10111684

patterns x 3 flights × 4 spectral bands) and 32 (4 correction methods × 2 flights × 4 × spectral bands) corrected images from each avocado and banana dataset, respectively. The reason we didn't apply irradiance normalisation to the banana data is due to the unstable performance on the avocado data, which will be discussed in the discussion section later. The conceptual workflow of the radiometric correction process is shown in Figure 4.

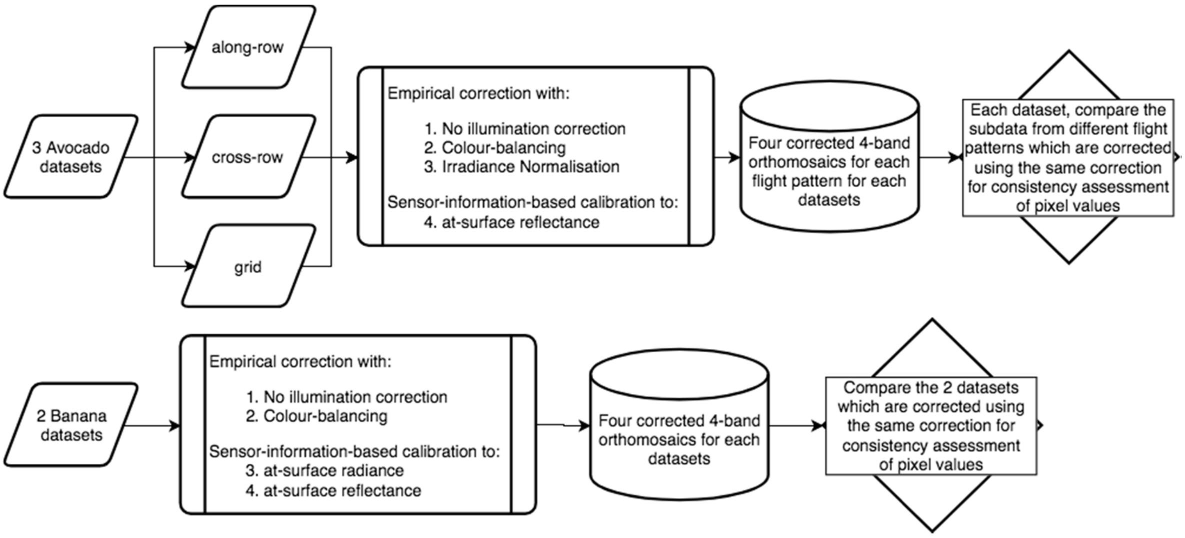

Figure 4 Conceptual workflow of the radiometric correction methods.

For method 1, Agisoft PhotoScan Pro was used to produce the orthomosaic with DN values. Its mosaic blending mode calculates weight for each match pixel and gives the pixel which projection vector is closest to the planar normal vector the highest weight. [22]. Blended digital numbers were automatically adjusted based on the camera dark current and sensitivity.

For method 2, we created a colour-balanced orthomosaic with DN values for the avocado data using Pix4DMapper and for the banana data using Agisoft PhotoScan Pro. This was because the colour-balancing feature was not included in the Agisoft PhotoScan Pro software at the time of processing the avocado data and we would like to keep the trees in the mosaic as similar to the original images as possible (see Figure 3). Nevertheless, these two software packages use the same algorithm for this task so similar pixel value patterns were observed. The algorithm generated the new DN value of object point k in image j based on the equation:

$$DN_{jk} = a_{rel_j} DN_{ik} + b_{rel_j} \tag{1}$$

where DN_{jk} is the DN value of object point k in adjacent image i; a_{rel_j} and b_{rel_j} are the applied coefficients to the reference image to ensure that the overlapping images are radiometrically homogeneous.

For method 3, an in-house Python code was used to extract the irradiance measurements recorded by the irradiance sensor and stored in the image metadata to normalise all raw images using the image with the lowest irradiance as the reference to avoid DN saturation. It adjusted the DN value based on a multiplier coefficient:

$$C_j(\lambda) = E_{ref}(\lambda)/E_j(\lambda) \tag{2}$$

where $E_{ref}(\lambda)$ is the irradiance measured in the reference image and $E_j(\lambda)$ is the irradiance measured in image *j*. By multiplying the DN value in image *j* with $C_j(\lambda)$, image *j* can be assigned the same irradiance level as the reference image. Afterwards, the irradiance-normalised images were imported into Agisoft PhotoScan Pro to create the irradiance-normalised orthomosaic.

For method 4, we generated the reflectance image directly based on the equation:

$$\rho = K f^2 \frac{(DN - B)G\Gamma}{(A\varepsilon\gamma + C)Count} \tag{3}$$

Peer-reviewed version available at Remote Sens. 2018, 10, 1684; doi:10.3390/rs10111684

where ρ is the reflectance, K is an unknown arbitrary number; f is the camera f-number, ε is the exposure time in seconds, γ is the ISO value; A, B, and C are calibration coefficients which are recorded in the metadata. $Count$, G, and Γ are parameters of the irradiance sensor, which represent arbitrary irradiance level, gain, and exposure time in seconds respectively. When processing, users can choose whether to enable irradiance input for such calculation. If there is no irradiance measurement or the irradiance measurement input was disabled in the software, the irradiance level is then assumed the same across all images. To get K, at least one known reflectance target is required within the image to solve the arbitrariness. Otherwise, the calculated reflectance would be in an arbitrary reflectance without normalisation. This equation can also be applied when there is no irradiance measurement. In this case, it is based on the assumption that the irradiance was a constant that can be part of K. If neither importing irradiance measurements nor solving K in equation (3), the calculated ρ would be surface radiance in an arbitrary unit, which is linearly correlated with $Wsr^{-1}m^{-2}$. This method is relatively novel for UAS image processing but very similar to the conventional way of processing satellite imagery [8]. Equation (3) was applied to convert both avocado and banana datasets to at-surface reflectance. At-surface radiance images were produced for the banana data only. It should be noted that equation (3) can only be applied to Parrot Sequoia products because different sensors use different conversion equations.

2.3.3 Correcting for Solar and Viewing Geometries Within and Between Images – Bidirectional Reflectance Distribution Function (BRDF)

Previous studies suggest that BRDF correction increases the brightness homogeneity of the mosaiced images for crop fields [13,14]. To address this we implemented a BRDF correction using the Walthal model [23] with an in-house Python script as a plugin of Agisoft PhotoScan Pro. For each pixel, it is assumed we can back-calculate their spatial location accurately as well as their projection on the earth after optimising camera positions and orientations with the aid of GCPs. Based on the known solar ephemeris, we can calculate the solar zenith and azimuth angles at a specific date and time for every pixel. Sensor view zenith and azimuth angles were calculated using the projection vectors from the camera centre to each pixel, then transform the vectors from the camera coordinates to the world coordinate system. With the known illumination and viewing angles, we can then use the parameters to solve a Walthal BRDF model using tie points as multiple observations. The Walthal BRDF model is described as:

$$r = a\theta_v^2 + b\theta_v \cos(\varphi_v - \varphi_s) + c \tag{4}$$

where r is the reflectance, θ_v is the viewing zenith angle, φ_v is the viewing azimuth angle, φ_s is the sun azimuth angle; and a, b, and c are the coefficients of the multivariate linear regression. We can calculate the nadir reflectance for the tie points by calculating the c value. In a horticultural environment, it is assumed there are usually two features on the ground: soil and vegetation. Therefore, we solved the Gaussian mixture model for each image and predicted which feature each pixel belonged to based on its DN value. The linear regression for each feature in each image based on the tie points' BRDF models was then calculated. By predicting which feature each pixel belonged to, a respective linear regression was applied to calculate the nadir reflectance for every pixel. For the avocado data, the BRDF correction was only applied to the generated orthomosaic with colour-balancing (method 2), following the recommendation of previously reported studies [13,14]. However, the BRDF correction algorithm was applied to the banana data with the sensor-information-based calibration (method 4), to explore a workflow which is similar to how at-surface reflectance is obtained from satellite imagery.

2.4. Assessment of canopy reflectance consistency

If it is possible to correct both internal and external errors due to canopy geometry and image orientation, then it should be possible to achieve similar results from the measurements which are conducted at the same time for the same features [16,24-26]. In other words, if a correction algorithm

Peer-reviewed version available at *Remote Sens.* **2018**, *10*, 1684; doi:10.3390/rs10111684

works properly, the corrected images from the temporally near-coincident datasets should provide consistent surface reflectance regardless of the variation in acquisition parameters.

It was difficult to guarantee that the distribution of pixel values would be similar in the same area from different datasets, due to the variations in observation perspectives among different flights caused by differences in flying height, speed and flying pattern. However, we can still compare the datasets' similarity in terms of calibrated pixel values using methods relying on simple statistical values such as box-and-whisker comparison. We compared the medians and interquartile range (IRQ) between two datasets to determine the likelihood of difference at the scale of objects, i.e. individual trees and patches of bare ground. If the two datasets did not have overlapping IRQs, we can confidently say that the two datasets are significantly different. If the IRQs are overlapping, then we can use the fraction of difference between medians (DBM) over overall visible spread (OVS) to determine whether there is a difference between two datasets. As C.J.Wild, *et al.* [27] suggested, the critical fraction to identify the difference of DBM/OVS are stated as follow:

1. For a sample size of 30, if this fraction is over 33%, there tends to be a difference.
2. For a sample size of 100, if this fraction is over 20%, there tends to be a difference.
3. For a sample size of 1000, if this fraction is over 10%, there tends to be a difference.

In this case the sample size is the pixel counts of the selected objects in the images. Based on the sample size and fraction values provided by [27], the critical fraction for the sample size between these provided numbers can be derived using the exponential relationship between the fraction criterion and the natural logarithm of the sample size as:

$$\text{critical fraction} = 2.6104 \times (\ln(sample\ size))^{-1.686} \tag{5}$$

This equation can help to determine the critical fraction for samples which have less than 1000 samples. Once the sample size reaches 1000, 10% is enough to determine that there tends to be a difference between two datasets. If the calculated DBM/OVS fraction had not exceeded the respective critical fraction, we concluded that there was no significant difference between the different input data. Thus, the estimated reflectance for selected feature was consistent between the datasets.

For the avocado data, we visually delineated the inner part of tree crowns for 17 selected trees and 15 ground areas and compared them between the images which were corrected with the same correction method from different flight patterns of the same flight. For the banana data, 15 trees and 10 ground areas were selected for the comparison between the images with the same correction method applied for the two datasets (**Error! Reference source not found.**). The delineated areas were saved as ESRI shapefiles and then batch processed using an in-house Python scripts for zonal statistics and to save the results to Microsoft Excel files for further analysis.

Figure 5 Selected trees and ground areas for both avocado (a) and banana (b) sites for box-and-whisker comparison

3. Results

In this section, we present the results of the calibrated reflectance consistency assessment with object-based box-and-whisker comparison for the avocado images. The box-and-whisker comparison results for the banana images will subsequently be presented. It should be highlighted that the analysis results in this section show the consistency of the calibrated reflectance rather than the absolute accuracy compared to other spectral measurements.

3.1. Reflectance consistency assessment of avocado imagery

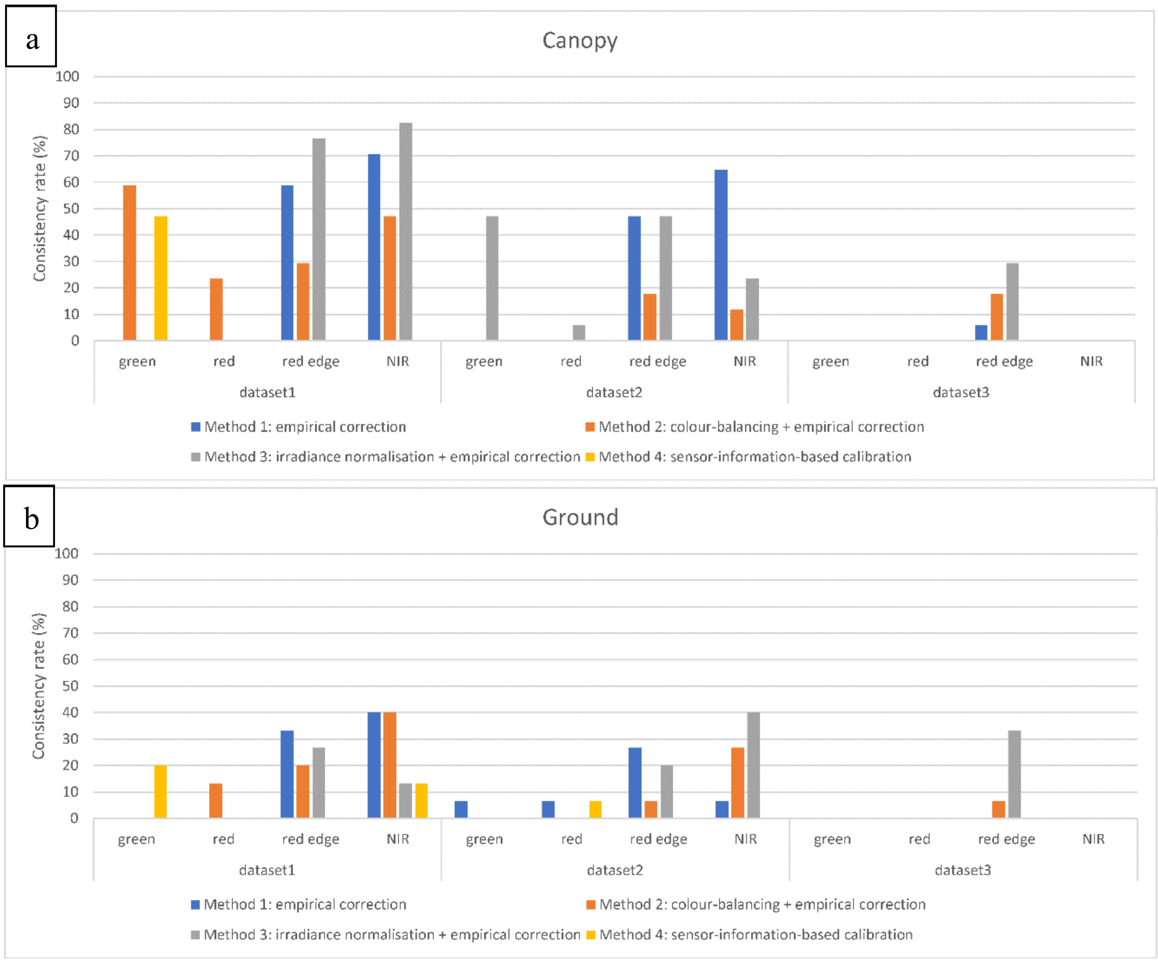

Figure 6 Consistency rate derived from box-and-whisker comparison for (a) canopy areas and (b) ground patches of avocado datasets. It only shows the lowest consistency rates among the three datasets because box-and-whisker comparison was only applicable on two datasets at a time. It shows that no method provided overall robust correction, while the consistency in the red edge and NIR bands is generally higher than in the green and red bands.

Error! Reference source not found. Figure 6 shows the consistency rate of the calibrated reflectance for the 17 selected tree canopies and 15 selected ground patches. Detailed comparison for tree canopies and ground areas can be found in Table A 1 to Table A 3 and Table A 4 to Table A 6 respectively. From Figure 6**Error! Reference source not found.**, we can tell that the reflectance consistency was much better for the canopy areas than the ground areas. Datasets 1, 2, and 3 have above ground flight altitudes of 75 m, 100 m, and 50 m, and solar elevation of approximately 60°, 80°, and 80° respectively. As mentioned before, we compared the sub-datasets which were the data with different flight patterns from the same flight. Therefore, since the tree canopy biophysical conditions did not change much during one flight, a high consistency percentage across all flight patterns was expected if a correction method was optimal. It is noted that the consistency rates of the red edge and NIR bands are mostly moderate and higher than the green and red bands, especially using the empirical-correction-based methods. However, it seems that no correction method provided an overall high consistency percentage for all bands in all datasets in this presented experiment. There is no correction method that provided consistently corrected reflectance values even for the canopy areas for dataset 3. The performance of colour-balancing and irradiance normalisation was not stable. Both of them increased the consistency rate in some of the datasets while decreased at the others.

3.2. Correction consistency assessment of banana imagery

Figure 7 shows the consistency rate of the radiometrically calibrated values between two temporally close datasets for the 15 selected tree canopies and 10 selected ground patches. Detailed information can be found in Table B 1**Error! Reference source not found.**. From Figure 7, we can tell that the calibrated values of canopies were more consistent than those for the ground areas, except for the NIR band using the simplified empirical correction. The consistency rates for the canopies in the red edge and NIR bands were generally higher than those for the green and red bands when the images were corrected with the empirical-correction-based method. It is noted that although the reflectance consistency rate was poor in the sensor-information-based calibration, the calibrated arbitrary radiance provided the highest consistency for the green and red bands.

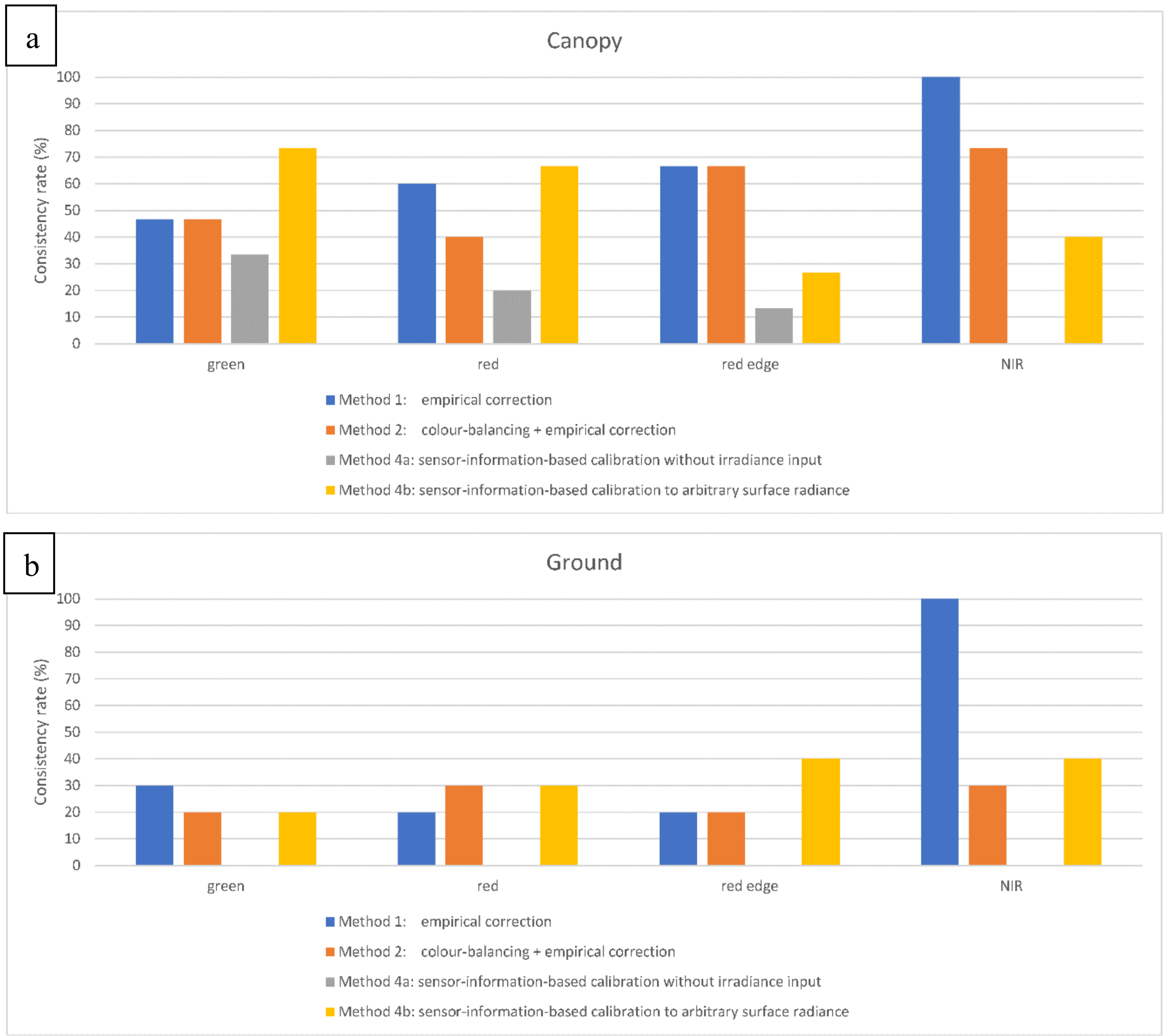

Figure 7 Consistency rate derived from box-and-whisker comparison for (a) canopy areas and (b) ground patches of banana datasets. The flight height is the same as avocado dataset 3 but the corrected values consistency is higher. The empirical-correction-based method provided higher consistency in red edge and NIR bands while sensor-information-based calibration provided higher consistency in green and red bands on canopies.

Peer-reviewed version available at *Remote Sens.* **2018**, *10*, 1684; doi:10.3390/rs10111684

3.3. BRDF correction consistency assessment

Figure 8 shows the estimated BRDF models for both canopy and ground features for an avocado orchard image in the NIR band. Both prediction models and Figure 9 show that most of the DN changes, where BRDF corrections were largest, occurred in the canopy areas. We analysed both single image brightness homogeneity and surface reflectance consistency to assess whether the proposed BRDF correction worked properly.

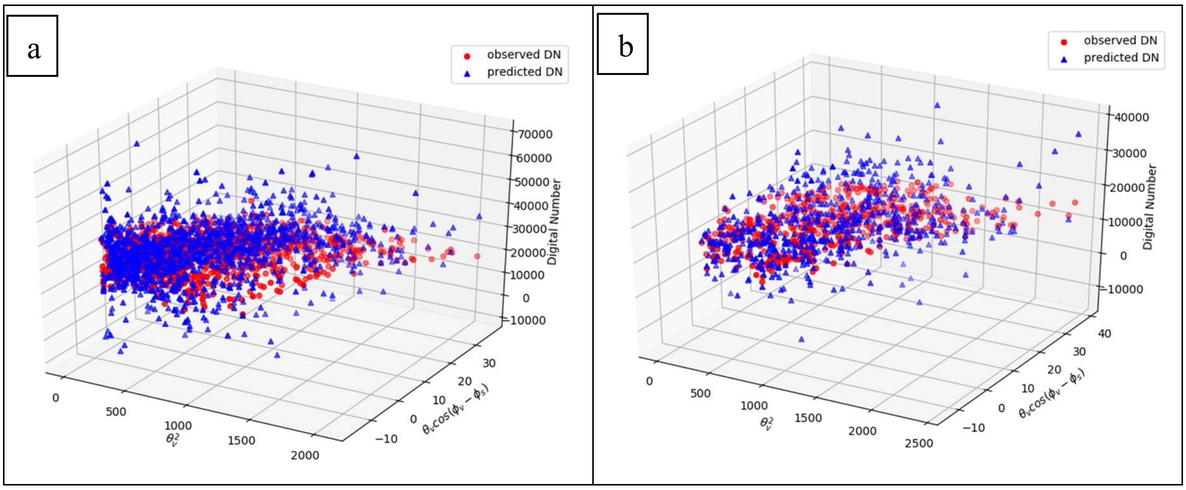

Figure 8 The diagrams show the predicted nadir DN versus observed DN by solving tie points' Walthal BRDF coefficients for the avocado image. (a) shows the scatterplot for canopy tie points, (b) shows the scatterplot for ground tie points. The x-axis represents squared viewing zenith angle, and the y-axis represents the viewing zenith angle multiply by the cosine of solar-viewing azimuth angle difference.

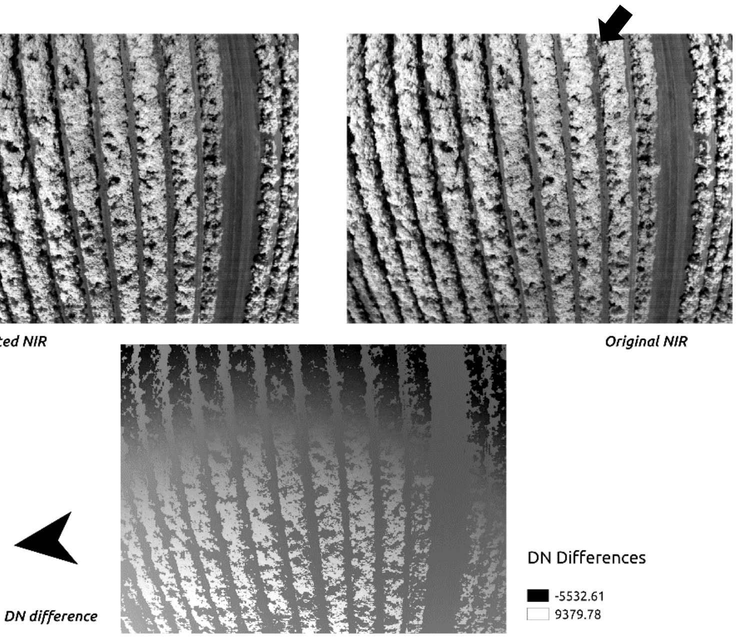

Figure 9 Image comparison before and after BRDF correction. The black arrow shows where the hot spot is.

We used an image which contained mostly ground feature and calculated the DN mean for every row and column and compared the covariance of rows and columns between the original image and corrected image to assess the single image brightness homogeneity for the avocado datasets. The larger the covariance was, the larger the DN values varied through the whole image. Results show

Peer-reviewed version available at *Remote Sens.* **2018**, *10*, 1684; doi:10.3390/rs10111684

that the covariance of the original image was 4409616 DN, whereas the covariance of the BRDF corrected image was 3864839 DN, which means the overall spread of DN distribution became smaller after BRDF correction. We also used the images containing the calibration panels at different locations in the images to compare the DN values difference. The black panel in the original images had a DN difference up to 6000 higher when the panel was near the image edge rather than at the centre, where the difference was reduced to around 1000 in the BRDF corrected images. These assessments were evidence that the proposed algorithm increased the brightness homogeneity. Increasing brightness homogeneity for the same features from different images can reduce brightness variation between similar features. From **Error! Reference source not found.**, we can tell that the hot spots in some of the avocado original images were eliminated after BRDF correction.

Table 1 Reflectance consistency percentages between different flight patterns in dataset 2

Correction method	Band	Along vs Cross	Along vs Grid	Cross vs Grid
BRDF + Colour balancing + Empirical correction on canopies	Green	0% (same)	0% (same)	5.9% (*better*)
	Red	0% (same)	0% (same)	0% (same)
	Red edge	52.9% (*better*)	88.2% (*better*)	64.7% (*better*)
	NIR	41.2% (*better*)	17.6% (worse)	64.7% (*better*)
BRDF + Colour balancing + Empirical correction on ground	Green	0% (same)	0% (same)	6.7% (*better*)
	Red	0% (same)	0% (worse)	26.7% (*better*)
	Red edge	0% (worse)	26.7% (*better*)	0% (worse)
	NIR	6.7% (worse)	6.7% (worse)	46.7% (*better*)

Table 2 Consistency assessment results for banana from box-and-whisker comparison between two temporally close flights

Correction method	Band	Canopies	Ground
BRDF + Sensor-information-based calibrated surface reflectance	Green	46.67% (*better*)	10% (*better*)
	Red	26.67% (*better*)	0% (same)
	Red edge	26.67% (*better*)	0% (same)
	NIR	33.33% (*better*)	0% (same)
BRDF + Sensor-information-based calibrated arbitrary surface radiance	Green	33.33% (worse)	10% (worse)
	Red	33.33% (worse)	40% (*better*)
	Red edge	53.33% (*better*)	0% (worse)
	NIR	20% (worse)	20% (worse)

Table 1 shows the results of the box-and-whisker plot comparison for assessing reflectance consistency between different flight patterns. The proposed BRDF correction did not improve the performance in the green and red bands. Compared to the result of colour balancing before the empirical correction in Table A 2 and Table A 5, the overall consistency increased a little bit in the red edge and NIR bands for canopies, although the difference was not significant. The consistency became even worse for the ground areas.

The results of the BRDF correction with sensor-information-based calibration for the banana datasets did not provide robust solutions either (Table 2). Although the consistency rate of at-surface reflectance increased by a maximum of 33% in NIR band, the consistency of the calibrated at-surface radiance dropped significantly in the green and red bands compared to the results in Table B 1.

To sum up, we found that for the avocado datasets, none of the proposed four correction methods provided consistent at-surface reflectance in the green and red bands. The empirical corrections provided moderate consistency rates in the red edge and NIR bands when the data was acquired above 75 m AGL. There is no evidence to prove that colour-balancing and on-board irradiance normalisation provided robust improvements in consistency rates, while the proposed

BRDF correction somehow improved consistency rates in the red edge and NIR bands for the canopy areas compared to the colour-balancing correction. For the banana datasets, we found that the empirical correction provided moderate consistency rates in the green and red bands even though the data was acquired at 50 m AGL. The consistency rates in the red edge and NIR bands were still higher, consistent with the observations for the avocado datasets. The sensor-information-based calibrated at-surface reflectance had the worst consistency rates in all bands. Nevertheless, the sensor-information-based calibrated arbitrary at-surface radiance showed the best consistency rates in the green and red bands. A brief comparison of the proposed methods performance can be found in Table 3**Error! Reference source not found.**.

Table 3 A simplified comparison table of the proposed correction methods. G, R, RE, and NIR are green, red, red edge, and NIR bands respectively. X means the method doesn't work well; V means the method works well; △ means the results are unstable; O means the results are moderately consistent. Diagonal lines mean the correction was not applied.

Correction method	Avocado datasets				Banana datasets			
	G	R	RE	NIR	G	R	RE	NIR
Simplified empirical correction	X	X	V	V	O	O	V	V
Colour-balancing + empirical correction	X	X	△	△	O	O	V	V
Irradiance normalisation + empirical correction	X	X	△	△				
Sensor-information-based calibrated reflectance	X	X	X	X	X	X	X	X
Sensor-information-based calibrated radiance					V	V	X	O
Remarks	None of them works when flight altitude is 50 m							

4. Discussion

4.1. The influences of flight altitude and image scale

There are several factors which affect the reflectance of tree canopies, such as viewed area, canopy geometry, terrain, and the viewing geometry between the ground surface, sensor, and the Sun [16]. As the spatial resolution increases, so does the variance of observed reflectance [16]. In addition, increasing spatial resolution in UAS imagery comes with lower flight altitude, which also means that each camera frame covers a smaller area. When creating orthomosaics for the same area with smaller image frames, higher variation in the illumination conditions and solar-viewing geometry will occur [9,13,14,16]. Therefore, the cause of the reflectance inconsistency in dataset 3 of the avocado orchard may be the due to the two factors. Besides, when pre-processing satellite images, the topographic effect caused by terrain is much more severe than individual features in the scene so that the canopy geometry variation can usually be simplified by simple physical models [28]. However, when the spatial resolution increases, the canopy geometry starts contributing to the variation in reflectance which is no longer negligible.

Moreover, it is well-known that the reflection properties of natural materials are usually scale-dependent [29]. In fine-scale imagery which is captured from an UAS, BRDF effect becomes more serious because of increasing Sun-surface-view geometry variation [16]. For correcting topographic effects for large-scale images, the Lambertian assumption is applied for most of the natural surfaces [29]. However, many studies have suggested that the BRDF models for natural surfaces are more sophisticated instead of being Lambertian [30-33]. Meanwhile, the diffusive illumination from the environment may affect the observed reflectance as well [29,34]. Such scattering from surroundings is easier to observe from the fine-scale measurement [34]. This factor may be the cause of inconsistent

Peer-reviewed version available at *Remote Sens.* **2018**, *10*, 1684; doi:10.3390/rs10111684

reflectance we found in our ground samples and some of the tree canopies. In a horticultural environment, trees are the majority in a scene and ground areas are surrounded by trees. Therefore, we suspect that higher possibility of diffusive light influenced the radiance the camera acquired, especially in the ground areas.

4.2. The influence of canopy geometric complexity on reflectance consistency

As mentioned above, the reflectance variation caused by canopy geometry becomes significant as the spatial resolution increases. This effect can be observed in the avocado datasets. Avocado datasets 2 and 3 had almost the same acquisition condition except for the flight altitude. Dataset 2 had a flight altitude of 100 m, which resulted in a 9.86 cm ground sample distance (GSD), whereas dataset 3 at a flight altitude of 50 m had a GSD of 4.74 cm. At such a high spatial resolution, we suspect that the effect of directional reflectance caused by leaf angle variation also started to contribute to radiometric distortion due to the reflection angle non-uniformity. In addition, such effect was more serious for the avocado orchard than for the banana plantation because the complexity of avocado tree crowns is much higher. The avocado dataset 3 had the same flight altitude as the banana datasets. However, there was no reflectance consistency in avocado dataset 3 while there was still some consistency observed in the banana datasets.

4.3. The limitation of simplified empirical correction

Studies have observed that the Parrot Sequoia multi-spectral camera has different sensitivity in different bands, and the maximum detectable reflectance for green and red bands are around 40% [35]. The saturation problem in the green and red bands reduces the effectiveness of empirical correction because it reduces the samples for calculating the linear regression. Moreover, the diffusive radiant flux in the horticultural environment may also cause the observed albedo of the calibration panels in the UAS images to be inaccurate, especially if the panels were deployed in a tree-surrounded area. Since the green and red bands are more sensitive, we suspect that the scattering of green and red radiant flux from the environment influenced the albedo measurement of the panels more seriously. Such characteristics can explain why the empirical correction always resulted in worse consistency in the green and red bands. Besides, the bidirectional reflectance phenomenon was also observed on the panels (see section 3.3). Perfectly Lambertian surface material are expensive so that we used a more cost-effective alternative which was proposed by Wang and Myint [10]. However, brightness variation in panels were still observed in some individual images. Except the possible diffusive flux influence, some of the brightness difference may be caused by backscatter as well.

In addition, the canopy geometric complexity of avocado trees also caused some problems when applying empirical corrections. The calibrated reflectance was very often negative in the green and red bands in avocado data when using empirical correction, but such negative reflectance problem was absent in the banana data using the same correction. We suspect that the complex canopy geometry caused many shaded leaves within tree crowns so that those shaded leaves became negative after applying empirical correction using panels. Besides, as previously mentioned, diffusive green and red radiant flux may increase the measured albedo on the panels so that created false relationship between pixel DN and at-surface reflectance. Setting the linear regression with a 0 interception could solve the negative values problem. However, it is not practical since the minimum DN value depends on the black current of the camera instead of zero. The negative reflectance will cause problem when we would like to derive vegetation indices from the reflectance. The solution is subtracting the minimum value which was found in the canopy areas (relevant to adding the value which has the maximum magnitude in negative domain) to the calibrated reflectance image as long as the reflectance still matches the spectral signature of vegetation.

4.4. UAS based Irradiance measurements

We also noticed that the irradiance measurements with the Sequoia® irradiance sensor had directional variation. In avocado dataset 1, the solar elevation was around 60°, and the flight direction

Peer-reviewed version available at *Remote Sens.* **2018**, *10*, 1684; doi:10.3390/rs10111684

was along-row, approximately aligning with the direction of the Sun. Comparing this with the subdataset from same dataset which was flown perpendicular to the Sun direction, the recorded irradiance measurements from adjacent images appeared with a 30% difference in its arbitrary irradiance unit, which is homogeneous to Wm^{-2}. Such difference may be the cause of unstable correction performance (see **Error! Reference source not found.**). Most of the modern onboard irradiance sensor for UAS equip with cosine corrector and was proved to increase the accuracy [36]. The lack of cosine corrector for Sequoia irradiance sensor may cause the measured irradiance being not direction independent. This is the reason that we didn't apply correction using irradiance measurement to the banana datasets, and neither input the irradiance measurement to the sensor-information-based calibration we used for the banana datasets.

4.5. Proposed BRDF correction

From Table 1, we can tell that the proposed BRDF correction did not improve the reflectance consistency. Part of the reason may be due to the limitation of the empirical correction we mentioned in section 4.3. However, from Table 2, we can tell that even without applying the empirical correction, the BRDF correction did not provide a robust solution for consistent measurements. Such inconsistency may be caused by non-uniform leaf inclination angle which is proved to impact the BRDF models [23,31]. Besides, some studies also suggested that the topographic effect on the BRDF models need to be addressed [16,29]. As we discussed in section 4.1, when the image becomes such fine-scale as UAS imagery, the non-uniform reflection properties caused by solar-surface-viewing geometry variation starts to affect the observation. Therefore, instead of only addressing the solar-viewing geometry as the proposed BRDF correction algorithm did, the surface topography also need to be considered for solving solar-surface-viewing geometry variation.

Another problem in our proposed algorithm is that solving the Gaussian mixture model of the pixel value distribution did not provide a good prediction to the objects in the images. Although there were usually two types of features in the scenes, there were many pixels in the canopies belonging to shaded leaves that were classified as ground features, and some pixels of the ground features which had hot spots that were classified as canopies. The wrong prediction of features resulted in the inappropriate linear regression being applied to those pixels. Consequently, such corrected images were very likely to make the correction more inconsistent. Since object detection using machine learning in UAS imagery has significantly progressed [37-39], we believe that this technology can possibly provide a robust solution to object detection. The correct object detection can help to solve the BRDF problem by providing the correct model to respective objects in the images. Such accurate object detection method can also help us to build empirical BRDF models for specific features in the images with enough input data. We believe that this will be a convenient way to deal with the BRDF problem.

4.6. Potential of sensor-information-based calibration

Although the sensor-information-based calibrated at-surface reflectance with panel input did not work very well (Figure 7), the arbitrary at-surface radiance from such calibration provided the best consistency in the green and red bands. The reason that the calibrated at-surface reflectance was not consistent may be caused by insufficient input to correlate the radiance to reflectance since this method only relies on one reflectance target to solve the arbitrariness instead of creating linear relationship in a range of reflectance. Besides, this calibration heavily relies on the coefficients provided by the manufacturers (Equation 3). This characteristic can explain that why the at-surface radiance consistency rates in red edge and NIR bands were not as high as green and red bands because the coefficients recorded in the firmware may not be as accurate. The behaviour of how captured radiance being converted to DN may also change after firmware update. Therefore, camera manufacturers should pay careful attention to identify the collected physical variables to calibrate the sensor to make sure the energy-to-signal conversion behaviour works as they expected [40,41]. Moreover, with the in-situ radiance measurement, camera end users could possibly calculate the conversion equation themselves to fit their needs in the local environments [40]. Once we can figure

Peer-reviewed version available at *Remote Sens.* **2018**, *10*, 1684; doi:10.3390/rs10111684

out accurate calibration parameters for a specific camera to get accurate surface radiance in $Wsr^{-1}m^{-2}$, it is possible to use either ground or onboard irradiance sensors to measure the irradiance in Wm^{-2} to calculate accurate surface reflectance.

5. Conclusions

Our results show that the bidirectional reflectance distribution function (BRDF) is an essential factor which needs to be taken into account to reduce brightness variations due to illumination and sensor geometries in UAS images. As discussed in sections 4.1 and 4.5, the fine-spatial scale characteristic in UAS imagery causes more serious BRDF effect. Past studies suggested using Walthal BRDF model to resolve the solar-viewing geometry variation [14]. However, in a more complex environment like orchard or even forest, the topography should also be considered to resolve the solar-surface-viewing geometry variation instead [29]. With enough input data, we can even build empirical BRDF models for features of interest and apply the respective models to different features in the images with the aid of object detection. Accurate BRDF model application should enable effective BRDF correction, which allows accurately mosaicking UAS images to provide more accurate analysis ready data for mapping and monitoring environmental changes.

Besides, the simplified empirical correction worked in some degree with conditions applied. Although the simplified empirical correction was proved to provide some good results in precision agricultural applications [9,11], for measuring trees which canopy geometry are complex, it is suggested that not acquiring the UAS imagery below a specific AGL because the smaller frame size and higher spatial resolution can increase the variation of solar-surface-viewing geometry. Some studies also suggested that flying the UAS at around 80 m AGL is the optimal protocol for measuring trees [4,42], which is very close to the height threshold we found for the avocado datasets. Besides, the surrounding environment of the calibration panels plays an important role to provide accurate reference. As we discussed in section 4.3, it should be as open and flat as possible to avoid diffusive radiant flux influence the observed albedo for the panels. Meanwhile, the reflectance design of the panels should also consider the radiant flux spectral sensitivity of camera to avoid signal saturation.

Meanwhile, the proposed illumination corrections, including colour-balancing and irradiance normalisation, didn't have stable performance in our experiment. Although colour-balancing were proved to improve brightness homogeneity in past studies [13,14], previous studies were conducted at a relatively homogenous environment and didn't assess its absolute accuracy. On the other hand, the lack of cosine corrector on the irradiance sensor makes the measured irradiance directional dependent. Therefore, in order to address a proper irradiance normalisation, accurate irradiance measurement should be conducted either on ground or onboard [13].

Finally, sensor-information-based calibration has potential to provide accurate reflectance. Although it didn't provide consistent result in our experiment, by calculating the accurate calibration coefficients, it is possible to convert the DN values to at-sensor radiance in $Wsr^{-1}m^{-2}$ directly. With simultaneously accurate measurement of irradiance in Wm^{-2}, the camera-measured at-surface radiance may be processed to at-surface reflectance directly. In addition, this calibration method takes photography factors into account so that it can reduce the possibility of brightness variation due to floating photography settings.

Radiometric correction protocols for satellite images are now commonly applied and the basis of analysis ready data for all mapping and monitoring, and correct images for illumination change, atmospheric effect, viewing geometry, and instrument response characteristics [43]. Although techniques for processing UAS multi-spectral imagery are relatively new, the general problem we need to deal with are still very similar except the scale is much smaller and the details of data are much higher. This study address what factors should be considered for radiometric correcting UAS multi-spectral imagery in order to analyse tree crop's biophysical properties and their temporal changes. The future related works can focus on addressing effective BRDF correction as well as establish a standard protocol for camera signal-to-radiance-to-reflectance conversion.

Peer-reviewed version available at *Remote Sens.* **2018**, *10*, 1684; doi:10.3390/rs10111684

Supplementary Materials: The following are available online at www.mdpi.com/xxx/s1, Figure S1: title, Table S1: title. All the Python scripts are available at author's GitHub: https://github.com/dobedobedo.

Author Contributions: Conceptualization, all the authors; Methodology, Yu-Hsuan Tu, Stuart Phinn, and Kasper Johansen; Software, Yu-Hsuan Tu.; Validation, Yu-Hsuan Tu; Formal Analysis, Yu-Hsuan Tu; Investigation, Yu-Hsuan Tu and Kasper Johansen; Resources, all the authors; Data Curation, Yu-Hsuan Tu; Writing-Original Draft Preparation, Yu-Hsuan Tu; Writing-Review & Editing, all the authors; Visualization, Yu-Hsuan Tu; Supervision, Stuart Phinn, Kasper Johansen, and Andrew Robson; Project Administration, Stuart Phinn; Funding Acquisition, Stuart Phinn and Andrew Robson.

Funding: This research was funded by Department of Agriculture and Water Resources, Australian Government as part of its Rural R&D for Profit Program's subproject "*Multi-Scale Monitoring Tools for Managing Australia Tree Crops - Industry Meets Innovation*".

Acknowledgments: The authors would like to acknowledge the support from local farmers, fieldwork assistants, and technical supports from online forums.

Conflicts of Interest: The authors declare no conflict of interest.

Appendix A Box-and-whisker comparison results of avocado datasets

Table A 1 Reflectance consistency percentages of tree canopies between different flight patterns in dataset 1

Correction method	Band	Along vs Cross	Along vs Grid	Cross vs Grid
Empirical correction	Green	41.2%	11.8%	0%
	Red	0%	0%	0%
	Red edge	58.8%	76.5%	76.5%
	NIR	82.4%	94.1%	70.6%
Colour balancing + Empirical correction	Green	58.8%	94.1%	88.2%
	Red	23.5%	88.2%	41.2%
	Red edge	29.4%	88.2%	70.6%
	NIR	47.1%	76.5%	82.4%
Irradiance normalisation + Empirical correction	Green	0%	47.1%	0%
	Red	0%	0%	0%
	Red edge	76.5%	70.6%	82.4%
	NIR	82.4%	94.1%	88.2%
Sensor-information-based calibration	Green	47.1%	100%	82.4%
	Red	0%	52.9%	0%
	Red edge	47.1%	0%	0%
	NIR	0%	88.2%	0%

Table A 2 Reflectance consistency percentages of tree canopies between different flight patterns in dataset 2

Correction method	Band	Along vs Cross	Along vs Grid	Cross vs Grid
Empirical correction	Green	0%	58.8%	0%
	Red	0%	11.8%	0%
	Red edge	64.7%	47.1%	88.2%
	NIR	64.7%	70.6%	76.5%
Colour balancing + Empirical correction	Green	11.8%	0%	0%
	Red	17.6%	0%	0%
	Red edge	47.1%	17.6%	52.9%
	NIR	11.8%	82.4%	11.8%
Irradiance normalisation + Empirical correction	Green	47.1%	58.8%	76.5%
	Red	23.5%	5.9%	5.9%
	Red edge	47.1%	70.6%	94.1%
	NIR	52.3%	82.4%	23.5%
Sensor-information-based calibration	Green	0%	0%	0%
	Red	0%	23.5%	0%
	Red edge	0%	100%	0%
	NIR	0%	88.2%	0%

Table A 3 Reflectance consistency percentages of tree canopies between different flight patterns in dataset 3

Correction method	Band	Along vs Cross	Along vs Grid	Cross vs Grid
Empirical correction	Green	0%	5.9%	0%
	Red	0%	58.8%	0%
	Red edge	5.9%	35.3%	5.9%
	NIR	5.9%	82.4%	0%
Colour balancing + Empirical correction	Green	0%	52.9%	0%
	Red	0%	17.6%	0%
	Red edge	23.5%	29.4%	17.6%
	NIR	0%	76.5%	0%
Irradiance normalisation + Empirical correction	Green	0%	0%	0%
	Red	0%	52.9%	0%
	Red edge	29.4%	52.9%	70.6%
	NIR	0%	88.2%	0%
Sensor-information-based calibration	Green	0%	5.9%	0%
	Red	0%	0%	0%
	Red edge	0%	88.2%	0%
	NIR	0%	64.7%	0%

Table A 4 Reflectance consistency percentages of ground areas between different flight patterns in dataset 1

Correction method	Band	Along vs Cross	Along vs Grid	Cross vs Grid
Empirical correction	Green	33.3%	0%	0%
	Red	0%	0%	0%
	Red edge	33.3%	60%	40%
	NIR	40%	66.6%	60%
Colour balancing + Empirical correction	Green	0%	0%	6.7%
	Red	13.3%	13.3%	20%
	Red edge	20%	40%	33.3%
	NIR	40%	73.3%	46.7%
Irradiance normalisation + Empirical correction	Green	33.3%	20%	0%
	Red	0%	6.7%	0%
	Red edge	26.7%	40%	26.7%
	NIR	13.3%	53.3%	33.3%
Sensor-information-based calibration	Green	40%	73.3%	20%
	Red	0%	53.3%	0%
	Red edge	6.7%	0%	0%
	NIR	13.3%	60%	6.7%

Table A 5 Reflectance consistency percentages of ground areas between different flight patterns in dataset 2

Correction method	Band	Along vs Cross	Along vs Grid	Cross vs Grid
Empirical correction	Green	26.7%	6.7%	26.7%
	Red	6.7%	6.7%	6.7%
	Red edge	66.7%	26.7%	40%
	NIR	13.3%	6.7%	60%
Colour balancing + Empirical correction	Green	0%	0%	0%
	Red	0%	6.7%	6.7%
	Red edge	33.3%	6.7%	26.7%
	NIR	26.7%	40%	26.7%
Irradiance normalisation + Empirical correction	Green	0%	26.7%	40%
	Red	0%	0%	20%
	Red edge	60%	40%	20%
	NIR	40%	46.7%	46.7%
Sensor-information-based calibration	Green	6.7%	0%	0%
	Red	13.3%	40%	6.7%
	Red edge	6.7%	53.3%	0%
	NIR	6.7%	40%	0%

Table A 6 Reflectance consistency percentages of ground areas between different flight patterns in dataset 3

Correction method	Band	Along vs Cross	Along vs Grid	Cross vs Grid
Empirical correction	Green	0%	0%	0%
	Red	0%	13.3%	0%
	Red edge	0%	40%	6.7%
	NIR	0%	93.3%	0%
Colour balancing + Empirical correction	Green	0%	20%	0%
	Red	20%	0%	0%
	Red edge	26.7%	6.7%	26.7%
	NIR	0%	46.7%	0%
Irradiance normalisation + Empirical correction	Green	0%	0%	0%
	Red	6.7%	6.7%	0%
	Red edge	40%	40%	33.3%
	NIR	0%	60%	0%
Sensor-information-based calibration	Green	0%	20%	0%
	Red	0%	0%	0%
	Red edge	0%	73.3%	0%
	NIR	0%	6.7%	0%

Appendix B Box-and-whisker comparison results of banana datasets

Table B 1 Consistency assessment results from the box-and-whisker plot comparison between two temporally close flights.

Correction method	Band	Canopies	Ground
Empirical correction	Green	46.67%	30%
	Red	60%	20%
	Red edge	66.67%	20%
	NIR	100%	100%
Colour balancing + Empirical correction	Green	46.67%	20%
	Red	40%	30%
	Red edge	66.67%	20%
	NIR	73.33%	30%
Sensor-information-based calibrated surface reflectance	Green	33.33%	0%
	Red	20%	0%
	Red edge	13.33%	0%
	NIR	0%	0%
Sensor-information-based calibrated arbitrary surface radiance	Green	73.33%	20%
	Red	66.67%	30%
	Red edge	26.67%	40%
	NIR	40%	40%

References

1. Zarco-Tejada, P.J.; Diaz-Varela, R.; Angileri, V.; Loudjani, P. Tree height quantification using very high resolution imagery acquired from an unmanned aerial vehicle (UAV) and automatic 3D photo-reconstruction methods. *European Journal of Agronomy* **2014**, *55*, 89-99, doi:10.1016/j.eja.2014.01.004.
2. Torres-Sánchez, J.; López-Granados, F.; Serrano, N.; Arquero, O.; Peña, J.M. High-Throughput 3-D Monitoring of Agricultural-Tree Plantations with Unmanned Aerial Vehicle (UAV) Technology. *PLoS ONE* **2015**, *10*, e0130479, doi:10.1371/journal.pone.0130479.
3. Herwitz, S.R.; Dunagan, S.; Sullivan, D.; Higgins, R.; Johnson, L.; Zheng, J.; Slye, R.; Brass, J.; Leung, J.; Gallmeyer, B. In *Solar-powered UAV mission for agricultural decision support*, Geoscience and Remote Sensing Symposium, 2003. IGARSS'03. Proceedings. 2003 IEEE International, 2003; IEEE: pp 1692-1694.
4. Johansen, K.; Raharjo, T.; McCabe, M. Using Multi-Spectral UAV Imagery to Extract Tree Crop Structural Properties and Assess Pruning Effects. *Remote Sensing* **2018**, *10*, 854, doi:10.3390/rs10060854.
5. Candiago, S.; Remondino, F.; De Giglio, M.; Dubbini, M.; Gattelli, M. Evaluating Multispectral Images and Vegetation Indices for Precision Farming Applications from UAV Images. *Remote Sensing* **2015**, *7*, doi:10.3390/rs70404026.
6. Comba, L.; Gay, P.; Primicerio, J.; Aimonino, D.R. Vineyard detection from unmanned aerial systems images. *Computers and Electronics in Agriculture* **2015**, *114*, 78-87, doi:10.1016/j.compag.2015.03.011.
7. Chianucci, F.; Disperati, L.; Guzzi, D.; Bianchini, D.; Nardino, V.; Lastri, C.; Rindinella, A.; Corona, P. Estimation of canopy attributes in beech forests using true colourdigital images from a small fixed-wing UAV. *International Journal of Applied Earth Observation and Geoinformation* **2016**, *47*, 60-68, doi:10.1016/j.jag.2015.12.005.
8. Jensen, J.R. *Introductory digital image processing : a remote sensing perspective*. 4th ed.. ed.; Glenview, IL : Pearson Education, Inc.: 2016.
9. Iqbal, F.; Lucieer, A.; Barry, K. Simplified radiometric calibration for UAS-mounted multispectral sensor. *European Journal of Remote Sensing* **2018**, *51*, 301-313, doi:10.1080/22797254.2018.1432293
10. Wang, C.; Myint, S.W. A Simplified Empirical Line Method of Radiometric Calibration for Small Unmanned Aircraft Systems-Based Remote Sensing *IEEE Journal of Selected Topics in Applied Earth Observations and Remote Sensing* **2015**, *8*, 1876-1885, doi:10.1109/JSTARS.2015.2422716.

11. Berni, J.A.J.; Zarco-Tejada, P.J.; Suárez, L.; Fereres, E. Thermal and Narrowband Multispectral Remote Sensing for Vegetation Monitoring From an Unmanned Aerial Vehicle. *IEEE Transactions on Geoscience and Remote Sensing* **2009**, *47*, 722-738, doi:10.1109/TGRS.2008.2010457.
12. Application Note: Pixel value to irradiance using the sensor calibration model. Parrot, Ed. Parrot: 2017; Vol. SEQ-AN-01.
13. Hakala, T.; Honkavaara, E.; Saari, H.; Mäkynen, J.; Kaivosoja, J.; Pesonen, L.; Pölönen, I. Spectral imaging from UAVs under varying illumination conditions. In *UAV-g2013*, Grenzdörffer, G.; Bill, R., Eds. International Society for Photogrammetry and Remote Sensing (ISPRS): Rostock, Germany, 2013; Vol. XL-1/W2, pp 189-194.
14. Honkavaara, E.; Saari, H.; Kaivosoja, J.; Pölönen, I.; Hakala, T.; Litkey, P.; Mäkynen, J.; Pesonen, L. Processing and Assessment of Spectrometric, Stereoscopic Imagery Collected Using a Lightweight UAV Spectral Camera for Precision Agriculture. *Remote Sensing* **2013**, *5*, 5006-5039, doi:10.3390/rs5105006.
15. Scarth, P. A methodology for scaling biophysical models. The University of Queensland, School of Geography, Planning and Architecture: 2003.
16. Wulder, M. Optical remote-sensing techniques for the assessment of forest inventory and biophysical parameters. *Progress in Physical Geography: Earth and Environment* **1998**, *22*, 449-476, doi:10.1177/030913339802200402.
17. Marceau, D.J.; Howarth, P.J.; Gratton, D.J. Remote sensing and the measurement of geographical entities in a forested environment. 1. The scale and spatial aggregation problem. *Remote Sensing of Environment* **1994**, *49*, 93-104, doi:10.1016/0034-4257(94)90046-9.
18. Novaković, P.; Hornak, M.; Zachar, M. *3D Digital Recording of Archaeological, Architectural and Artistic Heritage*. 2017, ISBN:978-961-237-898-1, doi:10.4312/9789612378981.
19. Application Note: How to correct vignetting in images. Parrot, Ed. Parrot: 2017; Vol. SEQ-AN-02.
20. Pix4D. Camera radiometric correction specifications. https://support.pix4d.com/hc/en-us/articles/115001846106-Camera-radiometric-correction-specifications (23 January, 2018),
21. Pasumansky, A. Topic: Questions about new calibrate color feature in 1.4. http://www.agisoft.com/forum/index.php?topic=8284.msg39660#msg39660 (23 January, 2018),
22. Pasumansky, A. Topic: About "Build Orthomosaic". http://www.agisoft.com/forum/index.php?topic=7000.0 (20 May, 2017),
23. Walthall, C.L.; Norman, J.M.; Welles, J.M.; Campbell, G.; Blad, B.L. Simple equation to approximate the bidirectional reflectance from vegetative canopies and bare soil surfaces. *Applied Optics* **1985**, *24*, 383-387.
24. Hapke, B. Bidirectional reflectance spectroscopy: 1. Theory. *Journal of Geophysical Research: Solid Earth* **1981**, *86*, 3039-3054, doi:10.1029/JB086iB04p03039.
25. Sellers, P.J. Canopy reflectance, photosynthesis, and transpiration, II. The role of biophysics in the linearity of their interdependence. *Remote Sensing of Environment* **1987**, *21*, 143-183, doi:10.1016/0034-4257(87)90051-4.
26. Moran, M.S.; Jackson, R.D.; Slater, P.N.; Teillet, P.M. Evaluation of simplified procedures for retrieval of land surface reflectance factors from satellite sensor output. *Remote Sensing of Environment* **1992**, *41*, 169-184, doi:10.1016/0034-4257(92)90076-V.
27. C.J.Wild; M.Pfannkuch; M.Regan; N.J.Horton. Towards more accessible conceptions of statistical inference. *Journal of Royal Statistical Society: Series A (Statistics in Society)* **2011**, *174*, 247-295, doi:10.1111/j.1467-985X.2010.00678.x
28. Dymond, J.R.; Shepherd, J.D. Correction of the Topographic Effect in Remote Sensing. *IEEE Transactions on Geoscience and Remote Sensing* **1999**, *37*, 2618-2620, doi:10.1109/36.789656.
29. Gu, D.; Gillespie, A. Topographic Normalization of Landsat TM Images of Forest Based on Subpixel Sun–Canopy–Sensor Geometry. *Remote Sensing of Environment* **1998**, *64*, 166-175, doi:10.1016/S0034-4257(97)00177-6.
30. Coulson, K.L.; Bouricius, G.M.; Gray, E.L. Optical reflection properties of natural surfaces. *Journal of Geophysical Research* **1965**, *70*, 4601-4611, doi:10.1029/JZ070i018p04601.
31. Verhoef, W.; Bach, H. Coupled soil–leaf-canopy and atmosphere radiative transfer modeling to simulate hyperspectral multi-angular surface reflectance and TOA radiance data. *Remote Sensing of Environment* **2007**, *109*, 166-182, doi:10.1016/j.rse.2006.12.013.
32. Gao, F.; Shaaf, C.B.; Strahler, A.H.; Jin, Y.; Li, X. Detecting vegetation structure using a kernel-based BRDF model. *Remote Sensing of Environment* **2003**, *86*, 198-205, doi:10.1016/S0034-4257(03)00100-7.

Peer-reviewed version available at *Remote Sens.* **2018**, *10*, 1684; doi:10.3390/rs10111684

33. Lucht, W.; Schaaf, C.B.; Strahler, A.H. An Algorithm for the Retrieval of Albedo from Space Using Semiempirical BRDF Models. *IEEE Transactions on Geoscience and Remote Sensing* **2000**, *38*, 977-998.
34. Goetz, A.F.H. *Making Accurate Field Spectral Reflectance Measurements*; ASD Inc.: Colorado, USA, 2012.
35. González-Piqueras, J.; Sánchez, S.; Villodre, J.; López, H.; Calera, A.; Hernández-López, D.; Sánchez, J.M. Radiometric Performance of Multispectral Camera Applied to Operational Precision Agriculture. Universidad de Castilla-La Mancha: Spain, 2018.
36. Bendig, J.; Gautam, D.; Malenovský, Z.; Lucieer, A. Influence of Cosine Corrector and UAS Platform Dynamics on Airborne Spectral Irradiance Measurements. Valencia, Spain, 2018.
37. Ma, X.; Geng, J.; Wang, H. Hyperspectral image classification via contextual deep learning. *EURASIP Journal on Image and Video Processing* **2015**, *2015*, 1-12, doi:10.1186/s13640-015-0071-8.
38. Cheng, G.; Han, J. A survey on object detection in optical remote sensing images. *ISPRS Journal of Photogrammetry and Remote Sensing* **2016**, *117*, 11-28, doi:10.1016/j.isprsjprs.2016.03.014.
39. Hung, C.; Bryson, M.; Sukkarieh, S. Multi-class predictive template for tree crown detection. *ISPRS Journal of Photogrammetry and Remote Sensing* **2012**, *68*, 170-183, doi:10.1016/j.isprsjprs.2012.01.009.
40. Del Pozo, S.; Rodríguez-Gonzálvez, P.; Hernández-López, D.; Felipe-García, B. Vicarious Radiometric Calibration of a Multispectral Camera on Board an Unmanned Aerial System. *Remote Sensing* **2014**, *6*, doi:10.3390/rs6031918.
41. Hiscocks, P.D. Measuring Luminance with a Digital Camera. Syscomp Electronic Design Limited 2011.
42. Dandois, J.P.; Olano, M.; Ellis, E.C. Optimal Altitude, Overlap, and Weather Conditions for Computer Vision UAV Estimates of Forest Structure. *Remote Sensing* **2015**, *7*, 13895-13920, doi:10.3390/rs71013895.
43. Lillesand, T.M.; Kiefer, R.W.; Chipman, J.W. *Remote sensing and image interpretation*. Seventh edition / Thomas M. Lillesand, Ralph W. Kiefer, Jonathan W. Chipman.. ed.; Hoboken, NJ : Wiley: 2015.